

PAPER • OPEN ACCESS

## Transition from elastic to plastic strain release in core–shell nanowires revealed by in-plane x-ray diffraction

To cite this article: Ali Al Hassan *et al* 2021 *Nanotechnology* **32** 205705

View the [article online](#) for updates and enhancements.



EEG/ECOG AMPLIFIERS  
& ELECTRODES  
ELECTRICAL/CORTICAL  
STIMULATORS  
REAL-TIME PROCESSING

**g.tec**  
gtec.at/shop  
**SHOP NOW**

# Transition from elastic to plastic strain release in core–shell nanowires revealed by in-plane x-ray diffraction

Ali Al Hassan<sup>1,2</sup> , Waheed A Salehi<sup>1</sup>, Ryan B Lewis<sup>3,4</sup> , Taseer Anjum<sup>1</sup>, Christian Sternemann<sup>5</sup>, Lutz Geelhaar<sup>4</sup> and Ullrich Pietsch<sup>1</sup>

<sup>1</sup>Naturwissenschaftlich-Technische Fakultät der Universität Siegen, D-57068 Siegen, Germany

<sup>2</sup>Institute for Photon Science and Synchrotron Radiation, Karlsruhe Institute of Technology, Hermann-von-Helmholtz-Platz 1, D-76344 Eggenstein-Leopoldshafen, Germany

<sup>3</sup>Department of Engineering Physics, McMaster University, Hamilton, Ontario L8S 4L7, Canada

<sup>4</sup>Paul-Drude-Institut für Festkörperelektronik, Leibniz-Institut im Forschungsverbund Berlin e.V., Hausvogteiplatz 5-7, D-10117 Berlin, Germany

<sup>5</sup>Fakultät Physik/DELTA, Technische Universität Dortmund, D-44221 Dortmund, Germany

E-mail: [ali.hassan@kit.edu](mailto:ali.hassan@kit.edu)

Received 12 November 2020, revised 25 January 2021

Accepted for publication 12 February 2021

Published 26 February 2021



CrossMark

## Abstract

We investigate the strain evolution and relaxation process as function of increasing lattice mismatch between the GaAs core and surrounding  $\text{In}_x\text{Ga}_{1-x}\text{As}$  shell in core–shell nanowire heterostructures grown on Si(111) substrates. The dimensions of the core and shell are kept constant whereas the indium concentration inside the shell is varied. Measuring the  $22\bar{4}$  and  $2\bar{2}0$  in-plane Bragg reflections normal to the nanowire side edges and side facets, we observe a transition from elastic to plastic strain release for a shell indium content  $x > 0.5$ . Above the onset of plastic strain relaxation, indium rich mounds and an indium poor coherent shell grow simultaneously around the GaAs core. Mound formation was observed for indium contents  $x = 0.5$  and  $0.6$  by scanning electron microscopy. Considering both the measured radial reflections and the axial 111 Bragg reflection, the 3D strain variation was extracted separately for the core and the  $\text{In}_x\text{Ga}_{1-x}\text{As}$  shell.

Keywords: core–shell nanowires, elastic strain investigation, plastic strain relaxation, synchrotron radiation, in-plane Bragg x-ray diffraction


(Some figures may appear in colour only in the online journal)

## Introduction

Compared to planar heteroepitaxy, the formation of axial or radial heterostructures in the form of nanowires has opened up new horizons for the design of heterostructures in a more efficient and less costly way [1–5]. One of the most beneficial qualities of core–shell nanowires is surface passivation of the core by the surrounding shell which can be utilized to

enhance the efficiency of photo-emission because it reduces non-radiative surface recombination [6, 7] and thereby enhances the opto-electronic properties of the device [8–10].

Strain relaxation in core–shell nanowires has been thoroughly investigated in recent years, revealing higher sustainability of elastic strain compared to planar heterostructures [11, 12]. Above a critical lattice mismatch between the core and shell materials, the misfit strain can relax via the formation of misfit dislocations [13, 14], quantum dots [15, 16] and stress-driven surface roughening [17, 18]. The aforementioned strain relaxation mechanisms within the nanowire core–shell system strongly depend on the diameter of the core, thickness of the shell and the lattice mismatch between the core and shell.

 Original content from this work may be used under the terms of the [Creative Commons Attribution 4.0 licence](https://creativecommons.org/licenses/by/4.0/). Any further distribution of this work must maintain attribution to the author(s) and the title of the work, journal citation and DOI.

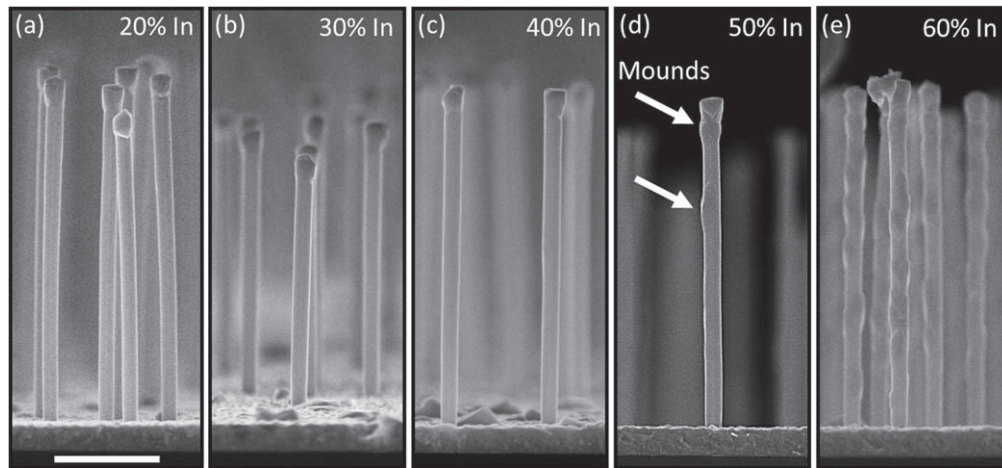


**Figure 1.** Panels (a)–(e) show SEM images of nanowires from samples 1–5, respectively. The scale bar in (a) is 1  $\mu\text{m}$  and applies to all SEM images.

For instance, Treu *et al* have reported that a 10 nm thick  $\text{InAs}_{0.91}\text{P}_{0.09}$  shell grows coherently around an InAs core. However, an InP shell of the same thickness shows the formation of dislocations [19]. Furthermore, it was revealed that the photoluminescence emission of this core–shell nanowire system exacerbates for higher P contents within the shell. This indeed indicates that the investigation of the strain relaxation mechanisms and critical composition of core–shell nanowires are of paramount importance for the fabrication of high performance devices with nanowire heterostructures.

Moreover, a novel strain relaxation process was recently revealed by Lewis *et al* 2017 [20] for GaAs nanowire cores surrounded by  $\text{In}_x\text{Ga}_{1-x}\text{As}$  shells. Based on lab x-ray diffraction of the axial 111 Bragg reflection and transmission electron microscopy measurements, it was demonstrated that above a critical lattice mismatch, plastically relaxed mounds form along the nanowire sidewall facets. The relaxed mounds and a coherent shell grow simultaneously from the beginning of  $\text{In}_x\text{Ga}_{1-x}\text{As}$  deposition such as, driven by strain relief, incoherent mound growth is increasingly favored for higher lattice mismatches. Furthermore, it was unveiled that the mounds are indium rich compared to an indium poor shell. However, Lewis *et al* did not measure the radial lattice parameters preventing 3D strain analysis.

In this work, we complement the above-described measurements by recording reciprocal space maps (RSMs) of the  $22\bar{4}$  and  $2\bar{2}0$  Bragg reflections which are orthogonal to the nanowire growth axis, and normal to the side edges and side-facets, respectively from GaAs/ $\text{In}_x\text{Ga}_{1-x}\text{As}$  core–shell nanowires with  $20\% \leq x \leq 60\%$  In. From these diffraction maps, on the one hand, we confirm the appearance of plastic strain relaxation for the highest In content of 60%, resulting in the simultaneous growth of indium rich mounds and an indium poor  $\text{In}_x\text{Ga}_{1-x}\text{As}$  shell, in agreement with [20]. However, the formation of mounds is observed for indium concentrations of 50% and above by scanning electron microscopy (SEM). We extend on these findings by calculating the 3D strain of the GaAs core and  $\text{In}_x\text{Ga}_{1-x}\text{As}$  shell at the edges and side-facets, revealing a strain variation of the

core which reaches its maximum for nanowires with 50% of indium in the  $\text{In}_x\text{Ga}_{1-x}\text{As}$  shell. Notably, for an indium concentration of 20%, the crystal lattice of the  $\text{In}_x\text{Ga}_{1-x}\text{As}$  shell at the side-facets and edges undergoes 3D compression whereas the GaAs core expands along and perpendicular to the growth direction regardless of the lattice mismatch.

## Experiment and results

The samples investigated in this work are GaAs/ $\text{In}_x\text{Ga}_{1-x}\text{As}$  core–shell nanowires grown by molecular beam epitaxy using the Ga-assisted vapor–liquid–solid growth on n-type Si(111) substrates covered by native oxide. The core diameter and shell thickness are kept constant at 140 nm and 18 nm respectively whereas the nominal indium concentration inside the shell is varied from 20% to 60% with steps of 10% for the five investigated samples (samples 1–5). A detailed description of the nanowire growth procedure can be found elsewhere [20]. SEM micrographs of nanowires from samples 1–5 are displayed in figure 1. The nanowires from samples 1–3 display a smooth surface whereas nanowires from samples 4–5 show exterior presence of mounds. However, the number density and relative size of the mounds is smaller for sample 4 (discussed later).

The x-ray diffraction measurements were carried out on as-grown nanowire ensembles at beamline BL9 [21] of the DELTA synchrotron (Dortmund, Germany) with 1  $\text{mm}^2$  beam and photon energy of 13 keV. To access the radial strain normal to the side facets and edges of the core and shell, rocking scans were performed in the vicinities of the  $22\bar{4}$  and  $2\bar{2}0$  in-plane Bragg reflections collecting the scattered intensity distribution using a two dimensional 100 k Pilatus detector placed 1 meter away from the sample. The experiment was executed in grazing incidence geometry where the angle of the incident beam with respect to the substrate surface was set to zero and the diffracted intensities of the  $22\bar{4}$  and  $2\bar{2}0$  Bragg reflections were measured in the plane perpendicular to the surface normal at Bragg angles at around

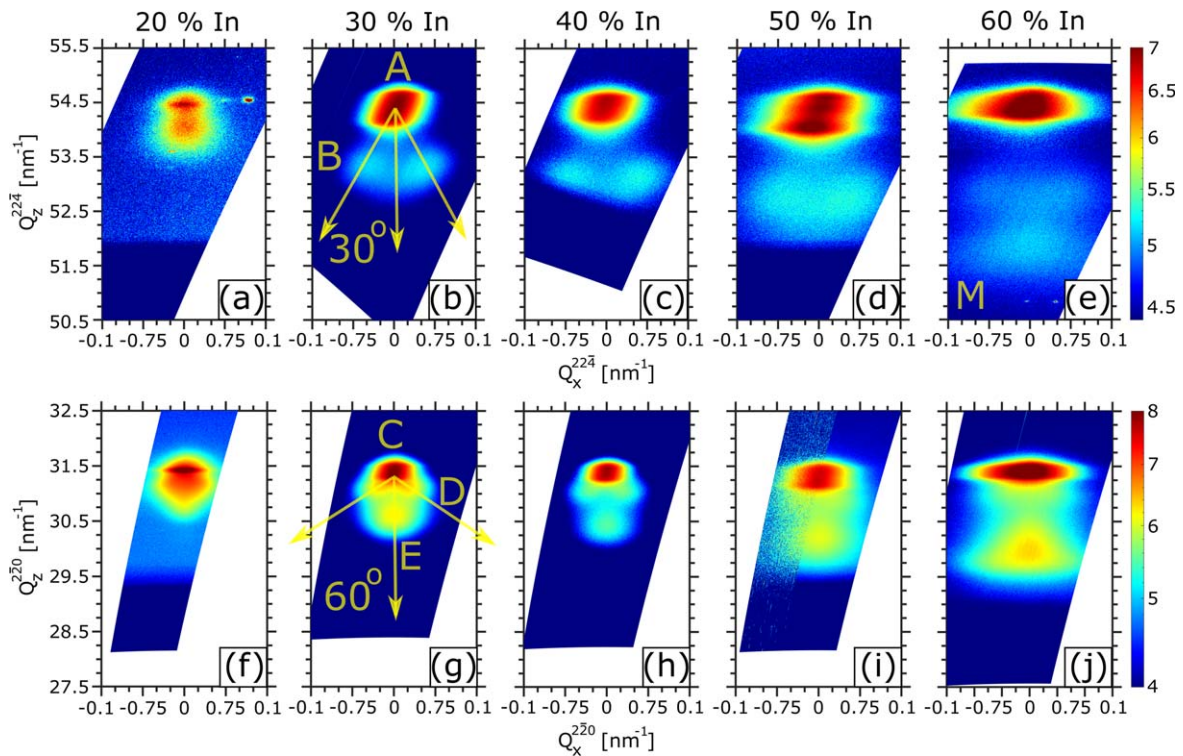


**Figure 2.** Panels (a)–(e) and (f)–(j) show RSMs of the  $22\bar{4}$  and  $\bar{2}20$  Bragg reflections for samples 1–5 respectively. All maps are plotted using the same color scale. The nominal indium concentration of each sample is mentioned on top of the each panel. Peaks A–E and M are explained in text.

$27.6^\circ$  and  $48.80^\circ$ , respectively. The 2D intensity frames collected at each rocking angle were integrated to compose 2D RSMs of the respective Bragg reflections. More information about the diffraction setup, and equations used to translate from real space angular coordinates into reciprocal space vectors can be found in [22]. From the width of a Si  $\bar{2}20$  substrate reflection measured at the same beamline under identical conditions (same beam energy, detector, sample to detector distance and beam size) an angular resolution of about  $0.05^\circ$  can be inferred.

RSMs of the  $22\bar{4}$  and  $\bar{2}20$  reflections are displayed in panels (a)–(e) and (f)–(j) of figure 2, respectively, ranging from samples 1 to 5 (from left to right). Reciprocal space vectors  $Q_z^{22\bar{4}}$  and  $Q_z^{\bar{2}20}$  are defined along the scattering direction of the measured planes in reciprocal space. In other words,  $Q_z^{22\bar{4}}$  and  $Q_z^{\bar{2}20}$  are sensitive to the variation in the spacing of the respective lattice planes. Reciprocal space vectors  $Q_{xx}^{22\bar{4}}$  and  $Q_{xx}^{\bar{2}20}$  are defined along  $[2\bar{2}0]$  and  $[22\bar{4}]$  respectively, and are sensitive to the nanowire tilt along the corresponding directions.

The scattering peaks, named A–E, in the RSMs of figures 2(b) and (g) can be explained by the strain impact on the lattice planes of different sections of the core–shell nanowire system [22–24]. For better clarity, a schematic correlation between the respective RSMs recorded for sample 2, and sketches of the core–shell nanowire cross-section overlapped by the  $22\bar{4}$  and  $\bar{2}20$  lattice planes are illustrated in figures 3(a) and (b). Peak A in the  $22\bar{4}$  RSMs originates from the  $22\bar{4}$  lattice planes of the GaAs core and the  $\text{In}_x\text{Ga}_{1-x}\text{As}$  side facets that are aligned vertically onto the side walls of the

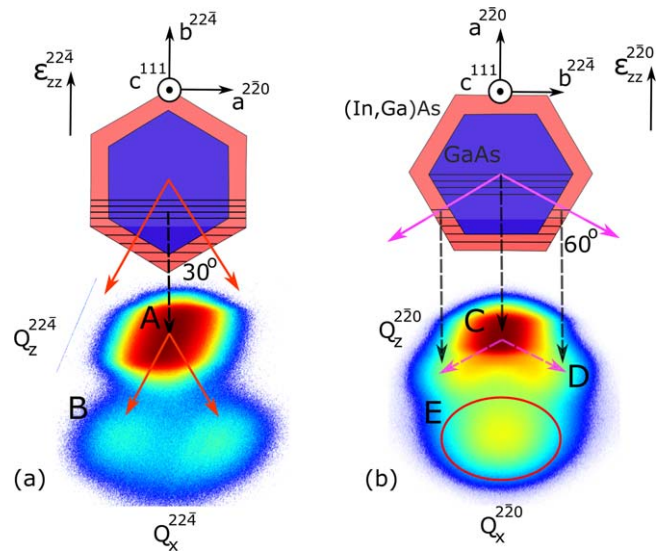


**Figure 3.** (a) and (b) Top rows show sketches of the core–shell nanowire cross-section oriented along  $Q_z^{22\bar{4}}$  and  $Q_z^{\bar{2}20}$ , illustrating the lattice planes of the respective reflections. RSMs of the  $22\bar{4}$  and  $\bar{2}20$  Bragg reflections of sample 2 are displayed in the bottom row. Peaks A–E are explained in text.

core in figure 3(a). The two sub-peaks B, indicated by red arrows at lower  $Q_z^{22\bar{4}}$  values, make an angle of  $30^\circ$  with  $[22\bar{4}]$  and therefore originate from the  $22\bar{4}$  lattice planes of the neighboring  $\text{In}_x\text{Ga}_{1-x}\text{As}$  side facets. The slight asymmetry in the intensity of the split peaks B for samples 2–4 (figures 2(b)–(d)), clearly seen in figure 3(a) for sample 2,



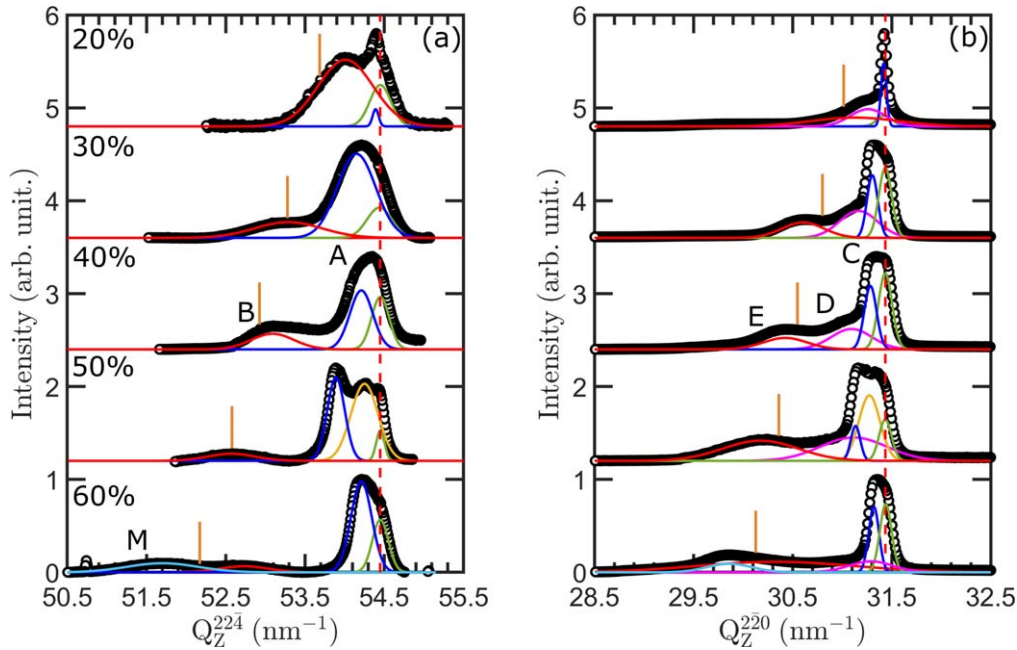


**Figure 4.** (a) and (b) show waterfall intensity integrations of the  $22\bar{4}$  and  $2\bar{2}0$  RSMs in figure 2. The red dashed lines at  $Q_z^{224} = 54.5 \text{ nm}^{-1}$  and  $Q_z^{220} = 31.5 \text{ nm}^{-1}$  indicate the positions of unstrained GaAs. The cut vertical orange lines represent the positions of unstrained  $22\bar{4}$  and  $2\bar{2}0$   $\text{In}_x\text{Ga}_{1-x}\text{As}$  for the nominal indium concentration of the sample. The colored Gaussian fits are explained in text.

where the peak on the right is more intense than the left one, can be attributed to the asymmetry of the (In,Ga)As shell i.e. the opposing side facets of the shell contributing to the right diffraction peak are thicker than the opposing side facets contributing to the left diffraction peak. This slight asymmetry can, in turn, result in a small nanowire bending which is responsible for the slanting of peak A for samples 2–4. The inhomogeneity of the shell may originate from the geometry of the evaporation sources with respect to the substrate in the growth chamber. Interestingly for sample 5, an additional sub-peak, labelled by M, is visible at low  $Q_z^{224}$  values (see figure 2(e)), presumably originating from the  $\text{In}_x\text{Ga}_{1-x}\text{As}$  mounds (see figure 1(e)). The same is expected for sample 4, as will be extended on later, but it is not visible due to the smaller scanning range (figure 2(d)). We attribute peak C in the  $2\bar{2}0$  RSMs to Bragg diffraction from the  $2\bar{2}0$  lattice planes of the GaAs core. Sub-peaks D, making an angle of about  $60^\circ$  with  $[2\bar{2}0]$ , are explained by diffraction from the  $2\bar{2}0$  lattice planes of neighboring  $\text{In}_x\text{Ga}_{1-x}\text{As}$  side facets. Peak E, indicated by a red circle in figure 3(b), belongs to the  $2\bar{2}0$  lattice planes of the measured couple of  $\text{In}_x\text{Ga}_{1-x}\text{As}$  opposite side facets that are aligned horizontally with the GaAs core.

Qualitatively, the central peaks appearing at  $Q_z^{224} = 54.5 \text{ nm}^{-1}$  and  $Q_z^{220} = 31.5 \text{ nm}^{-1}$  broaden along  $Q_z$  and  $Q_x$  for increasing nominal indium concentration in the  $\text{In}_x\text{Ga}_{1-x}\text{As}$  shell. The broadening along  $Q_z$  reflects the higher strain variation that the core undergoes whereas the broadening along  $Q_x$  resembles a higher angular tilt of the nanowires with respect to the substrate normal as the core–shell lattice mismatch increases. The broadest peak is observed for nanowires with 50% of nominal indium content. This is the transition point from elastic deformation to plastic strain

relaxation via the formation of  $\text{In}_x\text{Ga}_{1-x}\text{As}$  aggregates found by [20].

To estimate the strain variation in the core, the radial  $22\bar{4}$  and  $2\bar{2}0$  lattice constants and indium content of the  $\text{In}_x\text{Ga}_{1-x}\text{As}$  shell, we integrate the  $22\bar{4}$  and  $2\bar{2}0$  Bragg reflections along  $Q_x$  and fit the resulting  $Q_z$  line profiles, displayed in figure 4 with multi-Gaussians.

The red dashed lines at  $Q_z^{224} = 54.5 \text{ nm}^{-1}$  and  $Q_z^{220} = 31.5 \text{ nm}^{-1}$  in figure 4 indicate the positions of the respective unstrained lattice planes for GaAs. The cut vertical orange lines represent the positions of unstrained  $22\bar{4}$  and  $2\bar{2}0$   $\text{In}_x\text{Ga}_{1-x}\text{As}$  lattice planes for the nominal indium concentration of the sample. The red curves represent peaks B and E in  $22\bar{4}$  and  $2\bar{2}0$  respectively. The most intense peaks in  $22\bar{4}$  and  $2\bar{2}0$  are peaks A and C. Their broadening originates from the strain variation acting on the respective lattice planes of the GaAs core for peak C, and from the  $2\bar{2}0$  lattice planes of the core and the  $\text{In}_x\text{Ga}_{1-x}\text{As}$  facets which are aligned vertically on the sides of the core (see figure 3(a)) for peak A. Representing the lower and upper edges of this variation by the green and blue Gaussians, the strain variation can be calculated from the difference between these two peaks. The values of the strain variation calculated accordingly for the GaAs core for samples 1–5 are listed in table 1. The pink Gaussian peak along  $[2\bar{2}0]$  represents sub-peaks D. Conventionally, the Bragg peak of the substrate, supposed to be unstrained, is used as a reference to calculate the absolute strain in the nanowires. However, due to the absence of the Si peak in the in-plane diffraction pattern, we set the right edge of the core peak (colored in green in figure 4) to the position of unstrained GaAs for both  $22\bar{4}$  and  $2\bar{2}0$ . All other peaks have been shifted subsequently. This is an approximation because the GaAs core is affected by a small tensile strain induced by the surrounding shell

**Table 1.** Strain values along  $[22\bar{4}]$  and  $[2\bar{2}0]$  for the GaAs core (calculated with respect to unstrained GaAs from the blue curves using equation (1)) and the  $\text{In}_x\text{Ga}_{1-x}\text{As}$  shell and mounds (calculated with respect to unstrained  $\text{In}_x\text{Ga}_{1-x}\text{As}$  from the red and cyan curves using equation (1), and plotted in figure 5. The strain values along  $[111]$  are taken from [20].

In	$\varepsilon_{zz}^{22\bar{4}}$ (%)		$\varepsilon_{zz}^{2\bar{2}0}$ (%)		$\varepsilon_{zz}^{111}$ (%)
	Blue-Green	Red	Blue-Green	Red	
20%	$0.10 \pm 0.10$	$-0.62 \pm 0.92$	$0.05 \pm 0.12$	$-0.45 \pm 2.03$	0.45
30%	$0.55 \pm 0.63$	$-0.03 \pm 1.13$	$0.42 \pm 0.25$	$0.55 \pm 0.97$	0.70
40%	$0.44 \pm 0.38$	$-0.30 \pm 0.72$	$0.48 \pm 0.28$	$0.44 \pm 1.02$	0.96
50%	$1.02 \pm 0.29$	$-0.01 \pm 0.81$	$0.96 \pm 0.21$	$0.57 \pm 1.78$	0.74
60%	$0.44 \pm 0.34$	$0.96 \pm 1.22$ (mounds) $-1.00 \pm 0.83$ (shell)	$0.37 \pm 0.23$	$0.93 \pm 1.07$ (mounds) $-0.63 \pm 3.71$ (shell)	0.46

which results in a tiny shift towards lower  $Q_z$  values. However, this effect is neglected. The  $\text{In}_x\text{Ga}_{1-x}\text{As}$  shell of the nanowires in sample 1 is compressed as the red peak is centered at a higher  $Q_z^{22\bar{4}}$  value compared to the unstrained position assuming the nominal In content, which is indicated by a vertical cut line. For samples 2 (30% In) and 3 (40% In), the red Gaussian is almost centered at the  $Q_z^{22\bar{4}}$  values of unstrained  $\text{In}_{0.3}\text{Ga}_{0.7}\text{As}$  and  $\text{In}_{0.4}\text{Ga}_{0.6}\text{As}$  which leads to two possible explanations. The first is that the  $\text{In}_x\text{Ga}_{1-x}\text{As}$  shell is fully relaxed whereas the second is that the  $\text{In}_x\text{Ga}_{1-x}\text{As}$  shell is strained, but the tetragonal distortion is at an angle, so the compression and expansion mostly cancel out resulting in an average peak that is found at the unstrained  $Q_z^{22\bar{4}}$ . However, the  $2\bar{2}0$  Bragg reflection of the  $\text{In}_x\text{Ga}_{1-x}\text{As}$  shell being visible at lower  $Q_z^{2\bar{2}0}$  with respect to the unstrained value (peak E) indicates that the  $\text{In}_x\text{Ga}_{1-x}\text{As}$  lattice, in agreement with [20], is indeed strained and therefore negates the first explanation. For sample 5 (60% of indium), two peaks colored in red and cyan are visible along  $22\bar{4}$  and  $2\bar{2}0$ . The cyan peaks are at lower  $Q_z^{22\bar{4}}$  and  $Q_z^{2\bar{2}0}$  values compared to the unstrained position whereas the red Gaussians are at higher ones. This indicates that the  $\text{In}_x\text{Ga}_{1-x}\text{As}$  shell is indeed formed of two volumes with different indium concentrations higher and lower than 60%. As the nanowires of samples 4 and 5 show the formation of mounds at the nanowire surface (see figures 1(d) and (e)),  $\text{In}_x\text{Ga}_{1-x}\text{As}$  of sample 4 would be expected to be represented by two Bragg peaks, similar to sample 5. However, the relatively lower number density and smaller size of the  $\text{In}_x\text{Ga}_{1-x}\text{As}$  mounds of sample 4 (figure 1(d)) compared to those of sample 5 (figure 1(e)) indicate the early stage of mound formation and thereby the smaller impact the mounds have on the  $\text{In}_x\text{Ga}_{1-x}\text{As}$  shell. This will be expanded on in the discussion part.

The percentage lattice difference of the strained (In,Ga)As shell, mounds and GaAs core with respect to unstrained GaAs along  $[22\bar{4}]$  ( $\Delta b_{zz}^{22\bar{4}}$  (%)) and  $[2\bar{2}0]$  ( $\Delta a_{zz}^{2\bar{2}0}$  (%)) can be calculated from the peak positions extracted from the Gaussian curves (red and cyan for the (In,Ga)As shell and mounds, respectively; blue for the GaAs core) using the equation below,

$$\begin{aligned} \Delta b_{zz}^{hkl} (f \text{ or } hkl = 22\bar{4}) &= \Delta a_{zz}^{hkl} (f \text{ or } hkl = 2\bar{2}0) \\ &= \frac{Q_{\text{exp}}^{hkl} - Q_{0,\text{GaAs}}^{hkl}}{Q_{0,\text{GaAs}}^{hkl}} \times 100, \end{aligned} \quad (1)$$

where  $Q_{0,\text{GaAs}}^{hkl}$  is the position of unstrained GaAs along the respective  $[hkl]$  direction in  $Q_z$  and  $Q_{\text{exp}}^{hkl}$  is the experimental peak positions of the Gaussian curves. The results are plotted in figures 5(a) and (b).

The strain variation of the GaAs core is calculated from the blue curves using equation (1) since the green curves are already shifted to the position of unstrained GaAs ( $\varepsilon_z^{22\bar{4}} = \varepsilon_z^{2\bar{2}0} = 0$ ), and the strain acting on the  $\text{In}_x\text{Ga}_{1-x}\text{As}$  shell and mounds was calculated from the red and cyan curves replacing  $Q_{0,\text{GaAs}}^{hkl}$  by  $Q_{0,\text{In}_x\text{Ga}_{1-x}\text{As}}^{hkl}$  which is the position of unstrained  $\text{In}_x\text{Ga}_{1-x}\text{As}$  along the respective  $[hkl]$  direction in  $Q_z$ . The numerical strain values are listed in table 1 and plotted in figures 5(c) and (d).

The colors of the data points in figure 5 are correlated with those of the Gaussian fits in figure 4. As the green curves and cut orange lines in figure 4 were attributed to unstrained GaAs and  $\text{In}_x\text{Ga}_{1-x}\text{As}$ , the respective inplane strain values being zero were represented by horizontally stitched green and orange lines at  $\varepsilon_z^{22\bar{4}} = \varepsilon_z^{2\bar{2}0} = 0$  (figures 5(c) and (d)). On the one hand, looking at the separation between the blue data points and green lines, the strain variation in the core reaches a maximum of  $1.02 \pm 0.29\%$  and  $0.96 \pm 0.21\%$  along  $22\bar{4}$  and  $2\bar{2}0$  for the sample with 50% of indium content before decreasing down to  $0.44 \pm 0.34\%$  and  $0.37 \pm 0.23\%$  for the sample with 60% of indium. The values of the strain variation for samples 1–5 are listed in table 1. On the other hand, the strain acting on  $\text{In}_x\text{Ga}_{1-x}\text{As}$  is represented by the separation between the red data points and the cut orange lines (figures 4 and 5). The red data points of samples 2–4 being centered at positive  $\varepsilon_z^{2\bar{2}0}$  values (figure 5(d)) compared to  $\varepsilon_z^{22\bar{4}}$  reveal that the  $2\bar{2}0$  lattice planes of the  $\text{In}_x\text{Ga}_{1-x}\text{As}$  shell undergo higher expansion compared to the  $22\bar{4}$  lattice planes resulting from the compression along  $[111]$ . A similar higher lattice expansion along  $[2\bar{2}0]$  has been observed by Balaghi *et al* 2019 [25] for the GaAs cores when surrounded by thicker  $\text{In}_x\text{Ga}_{1-x}\text{As}$  shells. Interestingly, for sample 1, the  $\text{In}_x\text{Ga}_{1-x}\text{As}$  shell is compressed in all directions. For sample 5, the cyan and red data points at higher and lower values compared to  $\varepsilon_z^{22\bar{4}} = \varepsilon_z^{2\bar{2}0} = 0$  (see figures 4 and 5) are both associated with  $\text{In}_x\text{Ga}_{1-x}\text{As}$ . The first originates from an  $\text{In}_x\text{Ga}_{1-x}\text{As}$  volume with an indium concentration higher than 60% whereas the second shows a lower indium content. The TEM data for this

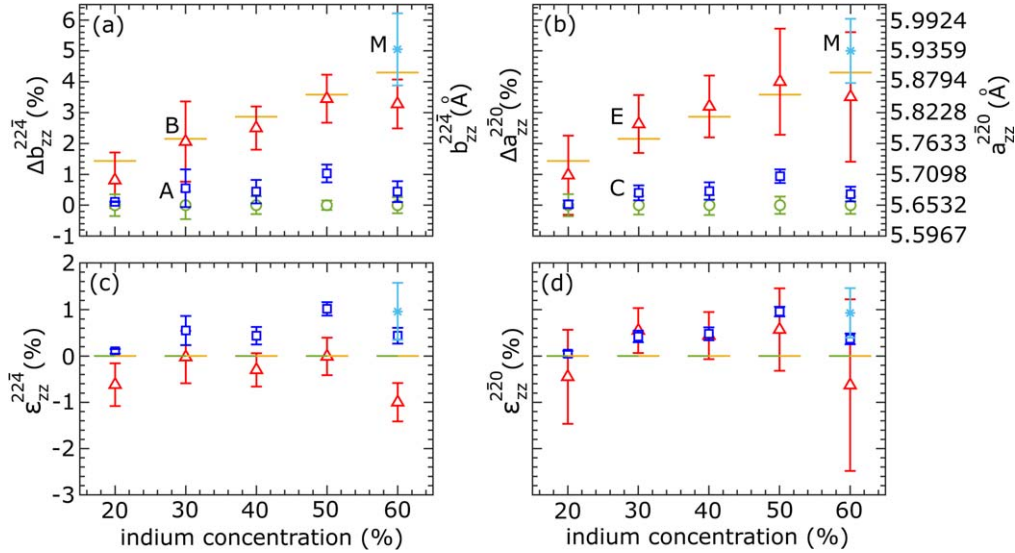


**Figure 5.** (a) and (b) display the percentage lattice difference of the strained shell, mounds and GaAs core with respect to unstrained GaAs along  $[22\bar{4}]$  ( $\Delta b_{zz}^{224}$  (%)) and  $[2\bar{2}0]$  ( $\Delta a_{zz}^{220}$  (%)). The spacing between the red dots and the orange cut lines represent the strain acting on the  $\text{In}_x\text{Ga}_{1-x}\text{As}$  shell as explained in the text below figure 4. The blue and green data points represent the right and left edges of the diffraction peak which originates from the core (figure 4). The cyan data points represent the  $\text{In}_x\text{Ga}_{1-x}\text{As}$  mounds for 60% of indium. The strain variation of the core and the strain acting on the  $\text{In}_x\text{Ga}_{1-x}\text{As}$  shell and mounds along  $[22\bar{4}]$  and  $[2\bar{2}0]$  are plotted in panels (c) and (d).

sample from Lewis *et al* indicated that the mounds are indium rich whereas the  $\text{In}_x\text{Ga}_{1-x}\text{As}$  shell, coherent to the core, is indium poor. The error bars were calculated taking into consideration the FWHM of the Gaussians as an input for equation (1).

To get a better understanding of the 3D strain behavior in the core and shell, we performed FEM simulations using a single nanowire model composed of a 140 nm thick GaAs core (blue colored volume in figure 6(a)) and 18 nm  $\text{In}_x\text{Ga}_{1-x}\text{As}$  shell with indium concentration of 30% (colored in red). More details about the numerical input, meshing procedure (figure 6(b)) and calculation scheme can be found in the FEM section of [24]. Iso-surface slices of the axial strain are demonstrated in figure 6(c) where apart from the upper section of the nanowire model, the core and shell share the same lattice parameter. Line profiles of the strain components  $\varepsilon_{2\bar{2}0}$  and  $\varepsilon_{22\bar{4}}$  (see figure 3 for orientation) extracted through one pair of opposite side facets and edges are displayed in the panels (d) and (e) of figure 6, respectively. In confirmation to our assumption, the  $\text{In}_x\text{Ga}_{1-x}\text{As}$  shell shows lattice expansion larger than the expected nominal lattice mismatch, as a result of the compression along the  $[111]$  direction. Interestingly, the inner section of the GaAs core shows slight expansion along  $[111]$ ,  $[2\bar{2}0]$  and  $[22\bar{4}]$ , faced by compression as one approaches the core-shell interface. For instance, for the nanowire model with 30% nominal indium concentration, the inner volume of the GaAs core undergoes a lattice expansion of 0.15% along  $[2\bar{2}0]$  and a maximum lattice compression of  $-0.20\%$  at the core-shell interface, forming a strain variation of 0.35%. This is in agreement with the strain variation deduced experimentally from the difference between the green and blue Gaussian peaks of 0.41%. This

experimental value might be overestimated because of normalization of the GaAs peak (see above).

## Discussion

The investigation of the strain behavior in nanowire heterostructures is essential for tuning the opto-electronic performance of the device. For instance, the strain induced by growing an  $\text{In}_x\text{Ga}_{1-x}\text{As}$  shell onto one side of a mismatched GaAs core has been utilized to control the bending radius of the nanowire [26] which would enable the realization of a complex spatially varying strain field opening up new possibilities for elastic strain and band structure engineering where the latter can be exploited to control the motion of charge carriers within the nanowire [26–28] and therefore tune its optical properties [29]. Moreover, GaAs nanowire cores exhibit reduction of their bandgap by up to 40% when overgrown with lattice-mismatched thick  $\text{In}_x\text{Ga}_{1-x}\text{As}$  shells [25].

Nevertheless, for high lattice mismatches (indium content 50% and above),  $\text{In}_x\text{Ga}_{1-x}\text{As}$  deposition around a thick GaAs core results in the simultaneous growth of an indium poor coherent shell and indium rich  $\text{In}_x\text{Ga}_{1-x}\text{As}$  mounds [20] (figures 1(d) and (e)). In the present work, this finding is confirmed by the presence of two  $\text{In}_x\text{Ga}_{1-x}\text{As}$  diffraction peaks along  $[22\bar{4}]$  and  $[2\bar{2}0]$  for sample 5 (red peak for the coherent shell and cyan peak for the mounds in figures 4 and 5). The lattice spacing of the mounds calculates to 5.9537 Å corresponding to a mismatch of  $\approx 5.3\%$  which is above the theoretical lattice mismatch considering 60% of indium by 1%. This reflects that the mounds are indeed indium rich compared to the  $\text{In}_x\text{Ga}_{1-x}\text{As}$  shell. The average indium



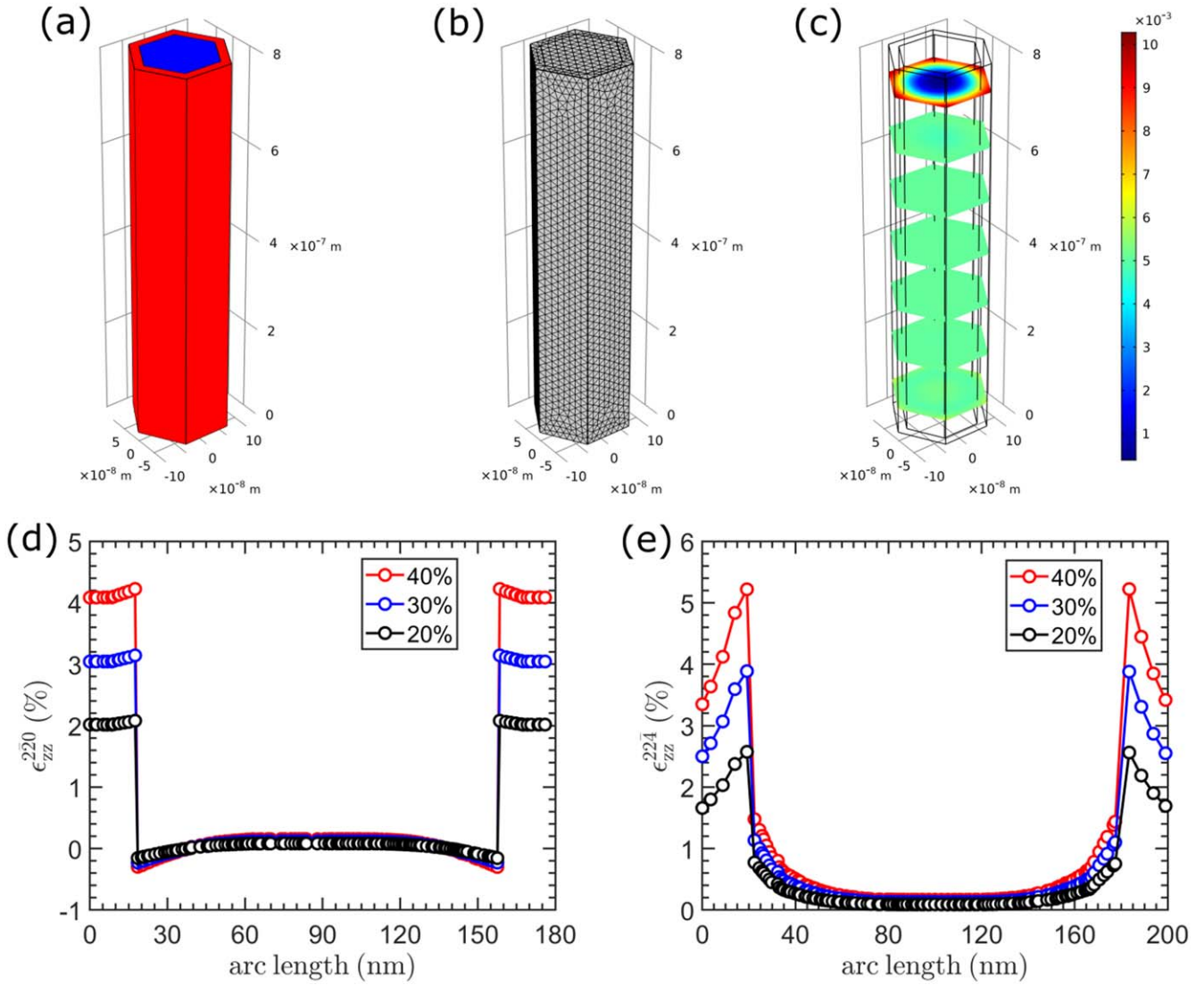


**Figure 6.** (a)–(c) show the core–shell configuration of the nanowire model, the mesh used and the slices of the axial strain along the nanowire axis, respectively. Panels (d) and (e) are line profiles of the strain components  $\epsilon_{220}$  and  $\epsilon_{224}$  extracted through the side facets and edges for samples 1–3, respectively.

concentration extracted from the cyan diffraction peaks in  $22\bar{4}$  and  $2\bar{2}0$  using Vegard's law is around 75%, which is reported to reach up to 80% in [20]. The indium enrichment of the mounds coincides with an indium depletion of the neighboring shell regions. The red Bragg peaks representing the coherent  $\text{In}_x\text{Ga}_{1-x}\text{As}$  shell translates into a mean indium concentration of 45%. However, the homogeneity of the indium distribution within the mounds depends on how indium diffuses from the shell into the mounds. In contrast to sample 5, sample 4 showed only one diffraction peak attributed to the shell and centered at the position corresponding to 50% of indium. This could be due to the short scan range in reciprocal space. However, an additional peak would be expected to be relatively less intense compared to that of sample 5. This could be attributed to the early stage of mound formation resembled by the relatively low number density and small size of the mounds (figure 1(d)) compared to those of sample 5 (figure 1(e)). Indeed, Lewis *et al* measured the

intensity of the relaxed  $\text{In}_x\text{Ga}_{1-x}\text{As}$  signal from the 111 Bragg reflection, demonstrating a constant value for 20%–40% of indium (attributed to parasitic growth on the substrate) and then an increase in the integrated intensity from 50%. The intensity between 50% and 60% doubles, reflecting the increasing mound volume with increasing In content.

The GaAs core undergoes a strain inhomogeneity, induced by the surrounding  $\text{In}_x\text{Ga}_{1-x}\text{As}$  shell, reflected by the broadening of its Bragg reflection along the scattering directions,  $Q_z^{224}$  and  $Q_z^{220}$ . As the indium content within the  $\text{In}_x\text{Ga}_{1-x}\text{As}$  shell increases from 20% to 50% (increasing lattice mismatch with constant core and shell dimensions), the strain variation acting on the core increases from  $(0.10 \pm 0.10\%)$  to  $(1.02 \pm 0.29\%)$  along  $[22\bar{4}]$  and from  $(0.05 \pm 0.12\%)$  to  $(0.96 \pm 0.21\%)$  along  $[2\bar{2}0]$ . Interestingly, as the nominal indium content increases to 60% (Sample 5), the GaAs core relaxes as the strain variation drops down to  $(0.44 \pm 0.34\%)$  along  $[22\bar{4}]$  and to  $(0.37 \pm 0.23\%)$  along  $[2\bar{2}0]$ . Absolute strain reduction has been observed axially for



the GaAs core in [20], and can be explained by the favored growth of the mounds rather than a coherent shell for an increasing core–shell lattice mismatch. The thinner the shell is, the less is the amount of strain induced on the core.

The  $\text{In}_x\text{Ga}_{1-x}\text{As}$  shell at the side-facet acts as a thin layer deposited on top of a GaAs substrate, which compresses along [111] and  $[2\bar{2}\bar{4}]$  ( $c^{111}$  and  $b_{(\text{In,Ga)As}}^{2\bar{2}0}$ ) to match the in-plane lattice spacing of the GaAs core ( $c^{111}$  and  $b_{\text{GaAs}}^{2\bar{2}0}$ ). This biaxial compression translates into expansion of  $\text{In}_x\text{Ga}_{1-x}\text{As}$  along  $[2\bar{2}0]$  ( $a_{(\text{In,Ga)As}}^{2\bar{2}0}$ ). This, indeed, has been experimentally validated and illustrated in figure 5 (red data points). However, for the nominal indium concentration of 20% (sample 2), the  $\text{In}_x\text{Ga}_{1-x}\text{As}$  shell seems to exhibit hydrostatic or tri-axial lattice compression, which is not understood. The complete opposite is expected for the GaAs core, which is supposed to undergo only slight expansion, due to its much larger volume, which increases when approaching the hetero-interface. Moreover, supported by the FEM simulations in figure 6, the GaAs core is expected to expand in all directions, being pulled apart by the surrounding lattice mismatched shell. Indeed, the GaAs core is simultaneously expanded axially and radially near the hetero-interface at the side-facets (blue data points in figure 5). Similar behavior has been reported before for thin GaAs cores surrounded by a relatively thick  $\text{In}_x\text{Ga}_{1-x}\text{As}$  shell [25].

Hetero-epitaxy of strained layers gives access to strain engineering. However, radiative recombination takes place at defect free strained layers only. Plastic strain relaxation associated with the formation of dislocations and other defects creates sources for non-radiative recombination of charge carriers [30] and reduce the luminescence intensity [31]. Considering Stranski-Krastanov growth mode known for lateral hetero-structures, there is a critical thickness beyond which misfit dislocations are created acting as non-radiative centers within the complete layer. In this study we demonstrate that in the case of GaAs/(In,Ga)As radial nanowire hetero-structures there exists also a critical indium concentration which changes the epitaxial growth. However, it is shown that a part of the shell remains coherently strained without dislocations where the strain is released through the formation of In rich mounds at the edges of the shell side-facets [20]. In consequence it means that the strained part still can provide radiative recombination as functional element of a respective optical device.

## Conclusions

In summary, sharing the same lattice parameter axially, the GaAs core and the  $\text{In}_x\text{Ga}_{1-x}\text{As}$  shell have different radial lattice spacings. This makes measuring in-plane Bragg reflections by XRD, namely 220 and 224 which are normal to the nanowire side-facets and edges, the perfect technique to perform a detailed investigation of the 3D strain behavior and variation in the core and the shell separately. Accordingly, we observed an increase in the average strain variation acting on the GaAs core when increasing the indium content from 10% to 50%, and strain relaxation for 50% and 60%. In addition,

for indium concentrations of 50% and 60%, simultaneous growth of relaxed indium rich mounds and an indium poor coherent shell takes place. These were represented by two diffraction peaks along  $[2\bar{2}\bar{4}]$  and  $[2\bar{2}0]$  for the sample with 60% of indium. However, one diffraction peak centered at the position corresponding to 50% of indium was evident for nanowires with nominal indium content of 50% in the shell, presumably due to the small volume of the mounds near the onset of mound formation and thereby the negligible impact on the shell. Furthermore, the lattice planes of the  $\text{In}_x\text{Ga}_{1-x}\text{As}$  shell showed relatively higher expansion along  $[2\bar{2}0]$  compared to  $[2\bar{2}\bar{4}]$ . Therefore, this technique is ideal for the investigation of the strain evolution and relaxation mechanism in nanostructures which can be correlated with further optical measurements.

## Acknowledgments

The authors would like to thank A-K Bluhm for the acquisition of SEM images and M Hörnicke as well as C Stemmler for maintenance of the molecular beam epitaxy system used for growth. We thank the DELTA machine group for providing synchrotron radiation at beamline BL9 and acknowledge Michael Paulus for support and discussions.

## Data availability statement

The data that support the findings of this study are available upon reasonable request from the authors.

## Funding

This work was supported by the Deutsche Forschungsgemeinschaft (grant no. Pi217/38). R.B.L. is grateful for additional funding from the Alexander von Humboldt Foundation.

## ORCID iDs

Ali Al Hassan  <https://orcid.org/0000-0002-2924-4215>

Ryan B Lewis  <https://orcid.org/0000-0002-7216-3541>

## References

- [1] Lauhon L, Gudiksen M, Wang D and Lieber C M 2002 *Nature* **420** 57–61
- [2] Royo M, De Luca M, Rurali R and Zardo I 2017 *J. Phys. D: Appl. Phys.* **50** 143001
- [3] Zhou C, Zhang X-T, Zheng K, Chen P-P, Matsumura S, Lub W and Zou J 2019 *Nanoscale* **11** 6859–65
- [4] Tomioka K, Yoshimura M and Fukui T 2012 *Nature* **488** 189–92
- [5] Tomioka K, Motohisa J and Fukui T 2020 *Sci. Rep.* **10** 10720
- [6] Treu J *et al* 2015 *Nano Lett.* **15** 3533–40

- [7] Ji X, Yang X, Du W, Pan H and Yang T 2016 *Nano Lett.* **16** 7580–7
- [8] Jiang X, Xiong Q, Nam S, Qian F, Li Y and Lieber C M 2007 *Nano Lett.* **7** 3214–8
- [9] van Tilburg J W W, Algra R E, Immink W G G, Verheijen M, Bakkens E P A M and Kouwenhoven L P 2010 *Semicond. Sci. Technol.* **25** 024011
- [10] Yang X, Shu H and Chen X 2016 *J. Alloys Compd.* **682** 571–8
- [11] Kavanagh K L 2010 *Semicond. Sci. Technol.* **25** 024006
- [12] Salehzadeh O, Kavanagh K L and Watkins S P 2013 *J. Appl. Phys.* **114** 054301
- [13] Dayeh S A *et al* 2013 *Nano Lett.* **13** 1869–76
- [14] Rieger T, Zellekens P, Demarina N, AlHassan A, Hackemüller F J, Lüth H, Pietsch U, Schäpers T, Grützmacher D and Lepsaa M I 2017 *Nanoscale* **9** 18392–401
- [15] Uccelli E, Arbiol J, Morante J R and Fontcuberta i Morral A 2010 *ACS Nano* **4** 5985–93
- [16] Yan X, Zhang X, Ren X, Lv X, Li J, Wang Q, Cai S and Huang Y 2012 *Nano Lett.* **12** 1851–6
- [17] Goldthorpe I A, Marshall A F and McIntyre P C 2008 *Nano Lett.* **8** 4081–6
- [18] Goldthorpe I A, Marshall A F and McIntyre P C 2009 *Nano Lett.* **9** 3715–9
- [19] Treu J *et al* 2013 *Nano Lett.* **13** 6070–7
- [20] Lewis R B, Nicolai L, Küpers H, Ramsteiner M, Trampert A and Geelhaar L 2017 *Nano Lett.* **17** 136–42
- [21] Krywka C, Paulus M, Sternemann C, Volmer M, Remhof A, Nowak G, Nefedov A, Pöter B, Spiegel M and Tolan M 2006 *J. Synchrotron Radiat.* **13** 8–13
- [22] AlHassan A, Davtyan A, Küpers H, Lewis R B, Bahrami D, Bertram F, Bussone G, Richter C, Geelhaar L and Pietsch U 2018 *J. Appl. Crystallogr.* **51** 1387–95
- [23] Stankevič T *et al* 2015 *J. Appl. Crystallogr.* **48** 344
- [24] AlHassan A *et al* 2018 *Phys. Rev. Mater.* **2** 014604
- [25] Balaghi L, Bussone G, Grifone R, Hübner R, Grenzer J, Ghorbani-Asl M, Krasheninnikov A V, Schneider H, Helm M and Dimakis E 2019 *Nat. Commun.* **10** 2793
- [26] Lewis R B, Corfdir P, Küpers H, Flissikowski T, Brandt O and Geelhaar L 2018 *Nano Lett.* **18** 2343–50
- [27] Jacobsen R S *et al* 2006 *Nature* **441** 199–202
- [28] Nam D, Sukhdeo D S, Kang J H, Petykiewicz J, Lee J H, Jung W S, Vucković J, Brongersma M L and Saraswat K C 2013 *Nano Lett.* **13** 3118–23
- [29] Treutlein P 2014 *Nat. Nanotechnol.* **9** 99–100
- [30] Tourbot G, Bougerol C, Grenier A, Den Hertog M, Sam-Giao D, Cooper D, Gilet P, Gayral B and Daudin B 2011 *Nanotechnology* **22** 075601
- [31] Consonni V, Knelangen M, Jahn U, Trampert A, Geelhaar L and Riechert H 2009 *Appl. Phys. Lett.* **95** 241910